

Fig. 3-1. A schematic of the UED experimental setup. Femtosecond UV pulses are used to both generate electrons in the electron gun as well as initiate the reaction in the molecular beam. Excitation pulses are time-delayed to obtain the time-resolved diffraction patterns.

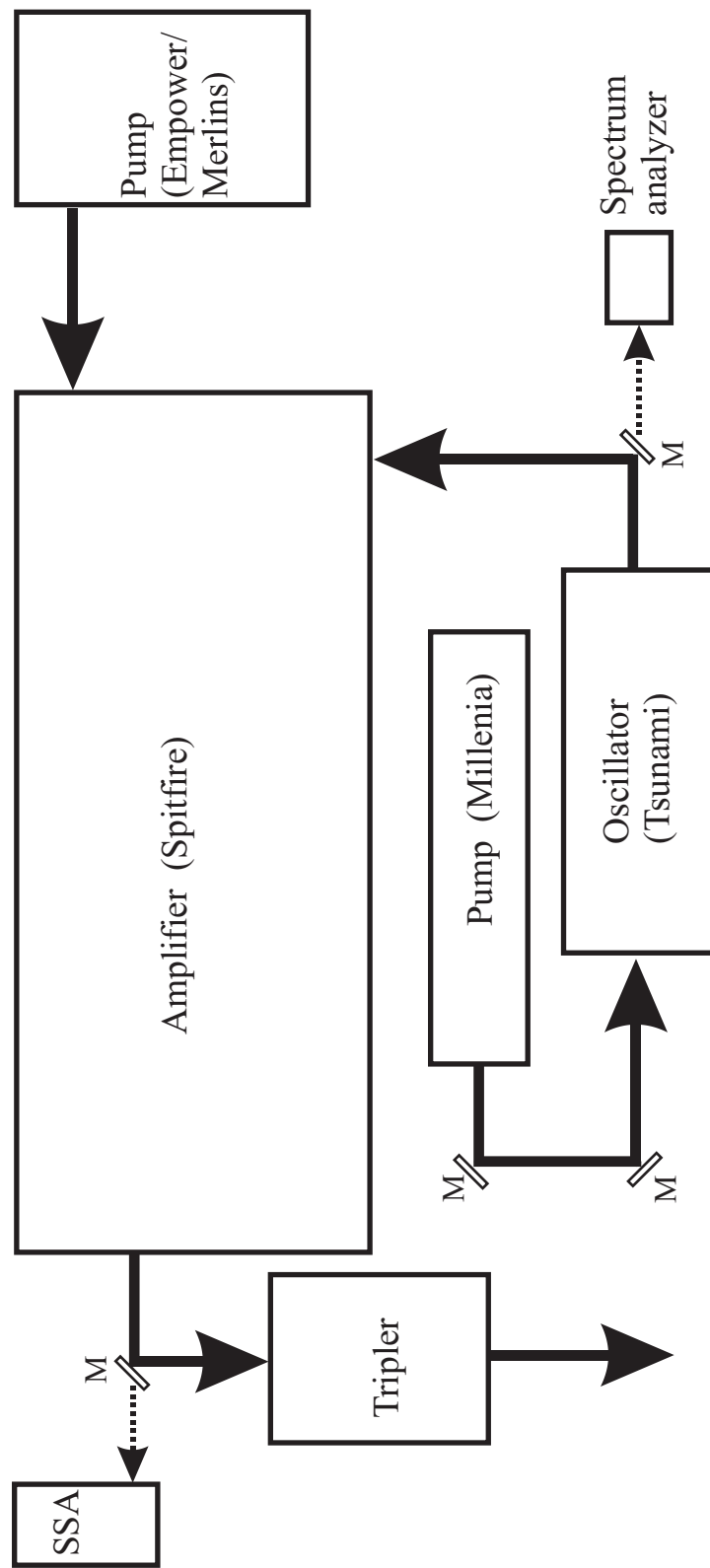


Fig. 3-2. Schematic of amplified femtosecond laser system used in UED experiments. Pulses from the oscillator are amplified by two stages of Ti:Sapphire gain. Amplified pulses are frequency tripled to yield the ultraviolet photons needed downstream. Bandwidth is monitored after the oscillator and the pulsewidth after the amplifier.

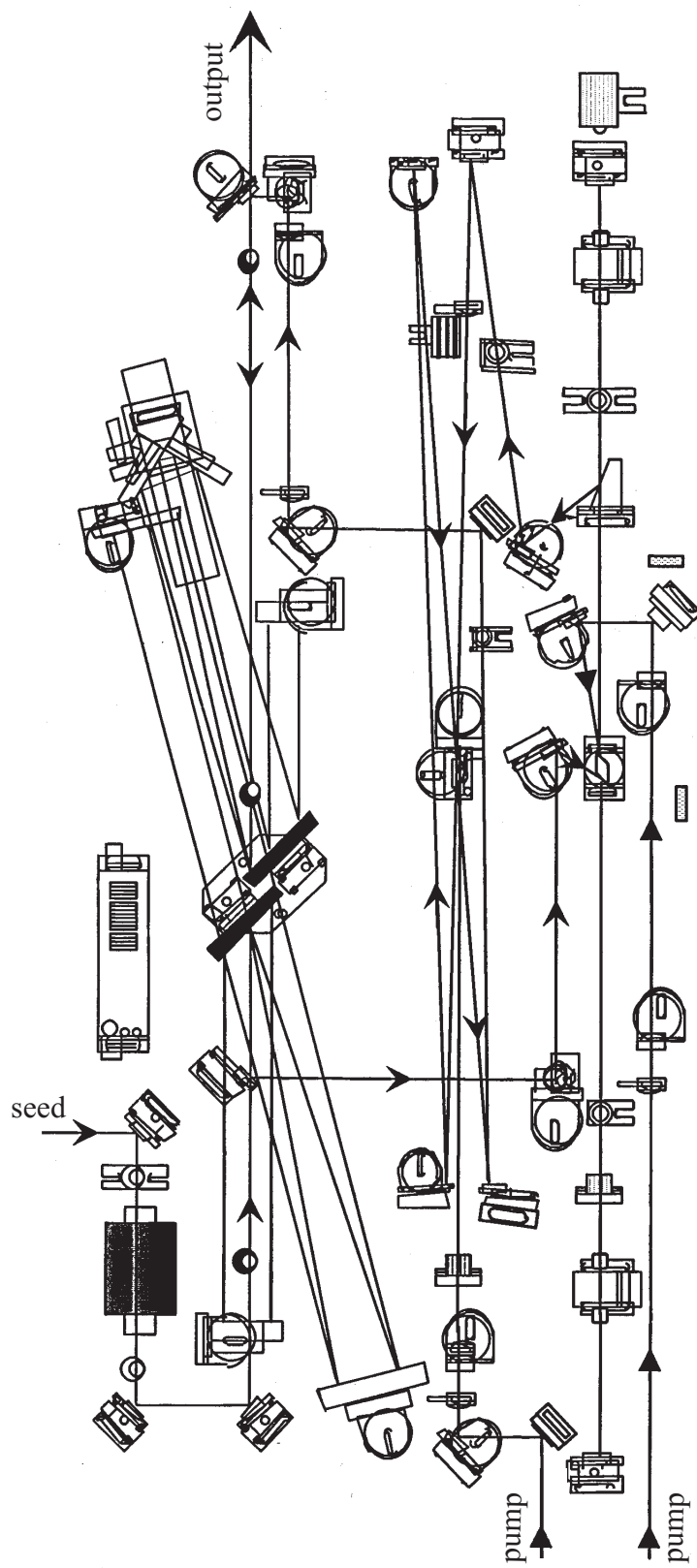


Fig. 3-3. Schematic of the chirped-pulse amplification system used to produce the high-energy infrared pulses. The pulses from the oscillator (seed) enter the amplifier and are temporally stretched before being amplified through two Ti:Sapphire stages-regenerative and multi-pass, each pumped by ~ 10 W of green light. Amplified pulses are then temporally compressed to about 120 fs before exiting the module. This figure is adapted from the SpectraPhysics Spitfire manual.

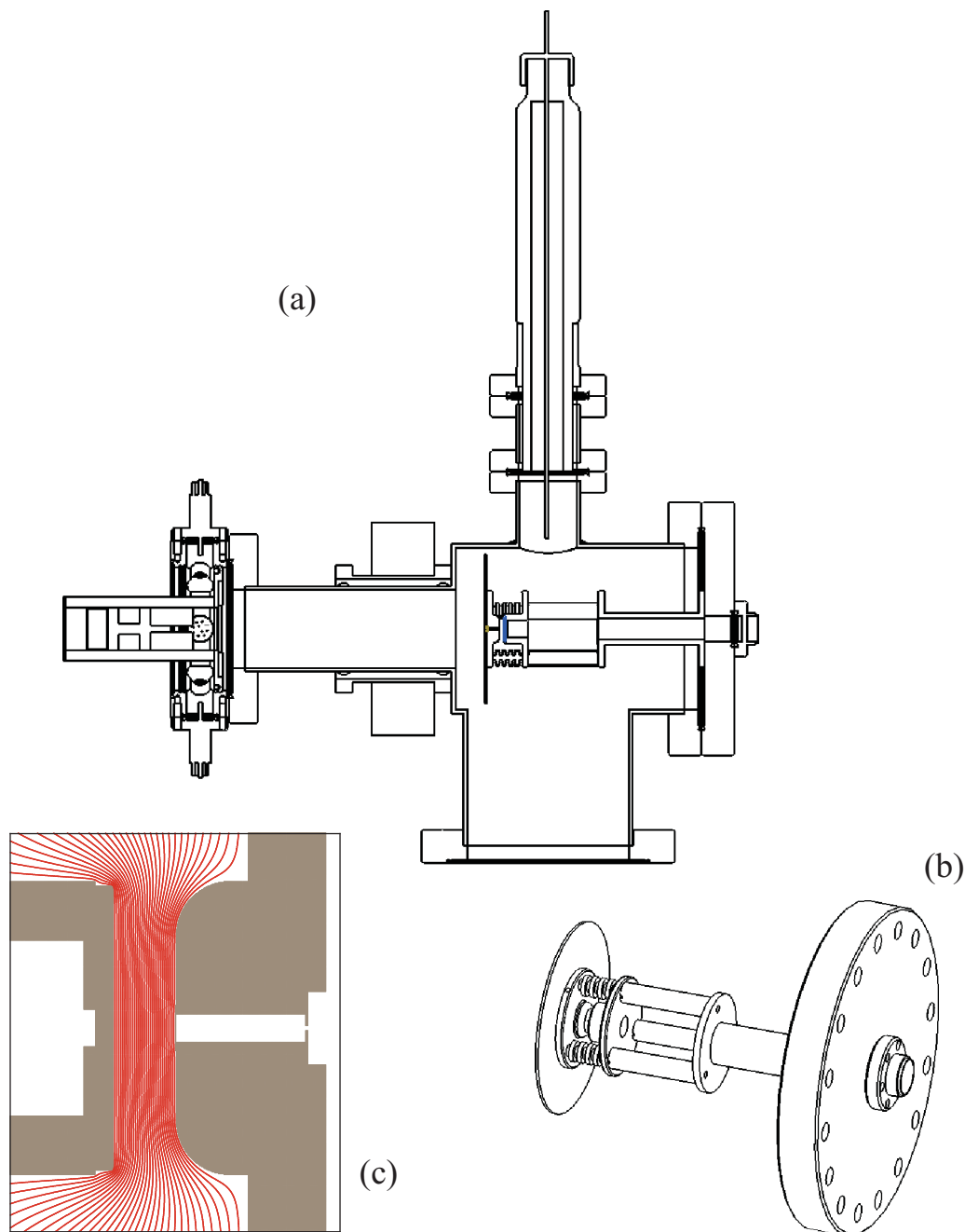


Fig. 3-4. The electron gun. (a) shows a cross-section of the entire gun. Laser pulses enter through the window at the right and strike the photocathode. Ejected electrons are accelerated toward the anode before passing through the magnetic lens and into the scattering chamber where the path of the beam may be manipulated by three pairs of charged plates. (b) The removable part of the electron gun containing the photocathode and anode. (c) Simulation showing the electric field lines between the cathode (left) and anode (right) at 30 kV potential.

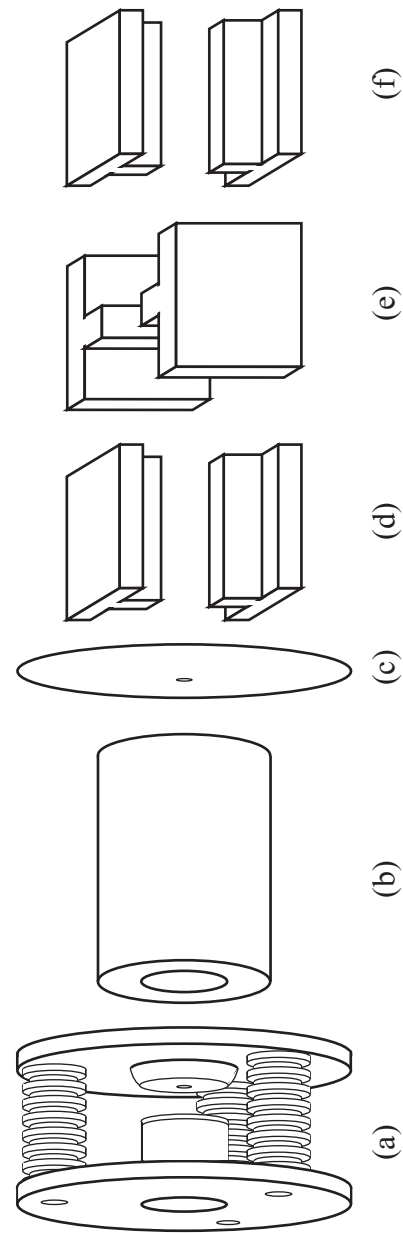


Fig. 3-5. Critical functional units of the electron gun. (a) The photocathode and anode separated (3 mm) by ridged Macor spacers. (b) A coil of wire comprising the magnetic lens. (c) A 2 mm hole separating the electron gun chamber from the main scattering chamber. (d) Vertical electrostatic deflection plates. (e) Horizontal electrostatic deflection plates. (f) Vertical electrostatic streaking plates.

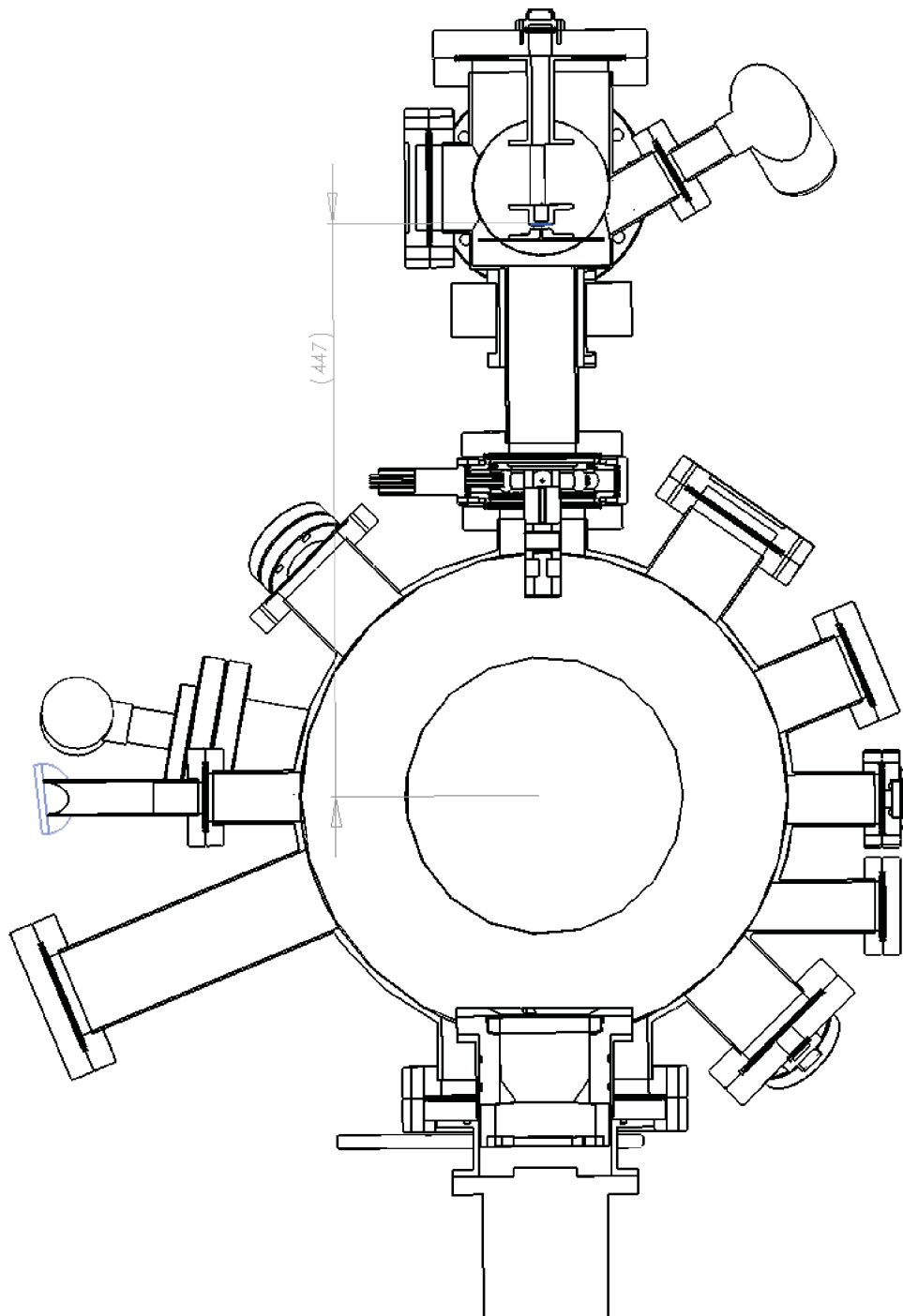


Fig. 3-6. Cross-section of the electron gun chamber (upper) and main scattering chamber (lower) showing a view from the top. The electrons are generated 447 mm from the interaction region at the center of the scattering chamber where electrons, laser, and molecular beam intersect in a mutually perpendicular alignment.

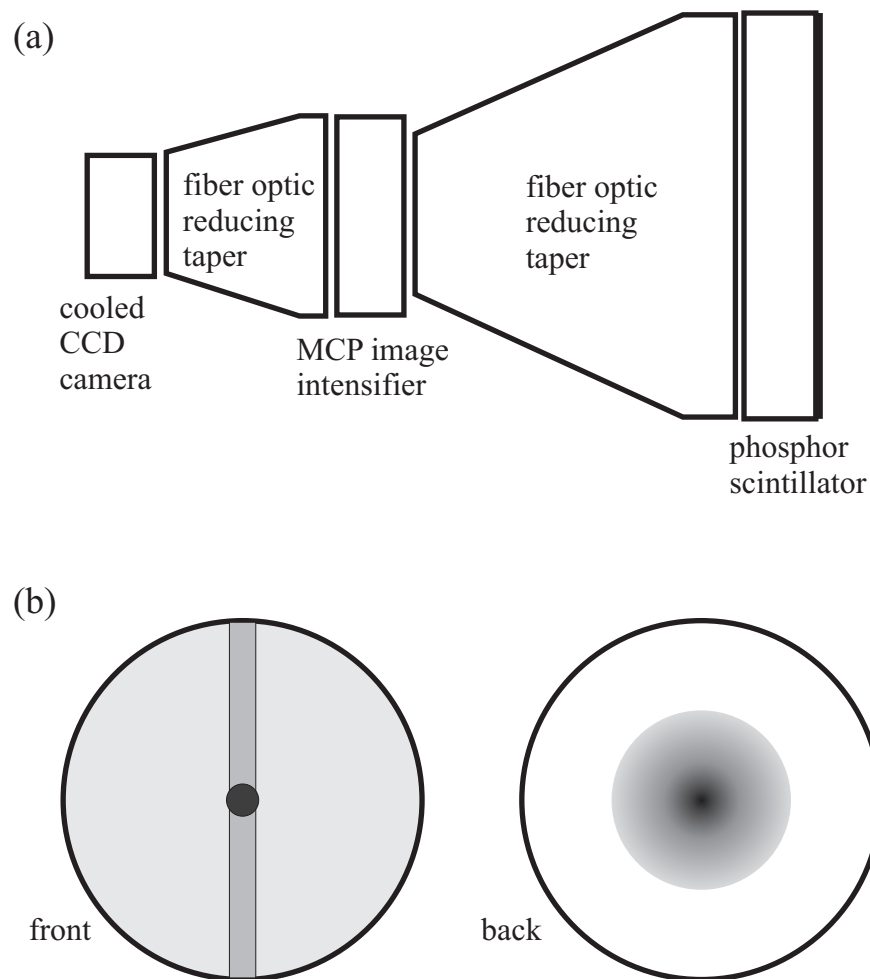


Fig. 3-7. (a) Schematic of the detection system showing the arrangement of component parts. Electrons strike the phosphor scintillator, resultant photons travel through a fiber-optic taper and are amplified by a microchannel plate (MCP) image intensifier. The amplified photons are detected by a cooled CCD chip. (b) Schematic of the phosphor scintillator showing the aluminum strip and Faraday cup on the front and the variable neutral-density filter on the reverse.

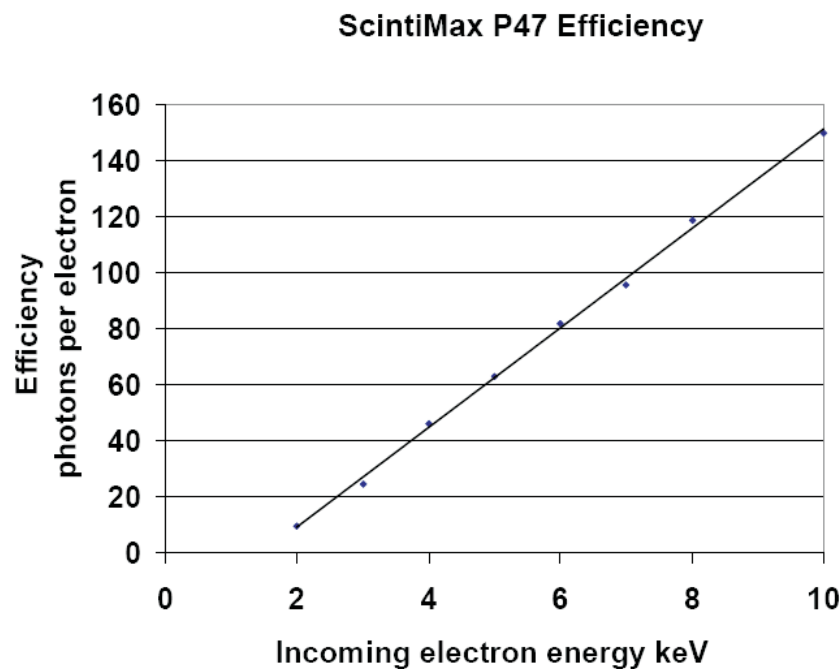


Fig. 3-8. The efficiency of P-47 phosphor (the type used in UED). Extrapolated to 30 keV, one impinging electron should spawn about 500 photons. Data from El-Mul Technologies, Ltd.

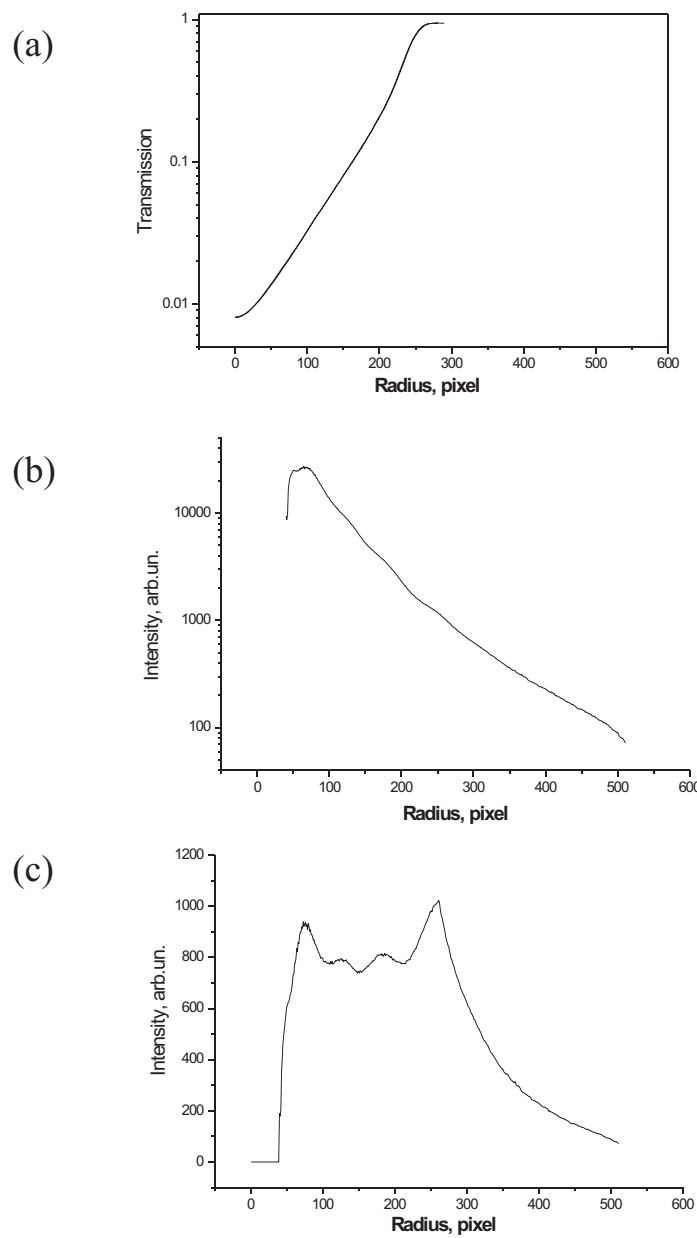


Fig. 3-9. (a) The effect of the radial symmetric filter on the transmission through the fiber-optic face plate. (b) The unfiltered one-dimensional scattering signal of trifluoromethyl iodide. (c) The filtered one-dimensional scattering signal of trifluoromethyl iodide showing the increase in dynamic range of detection.

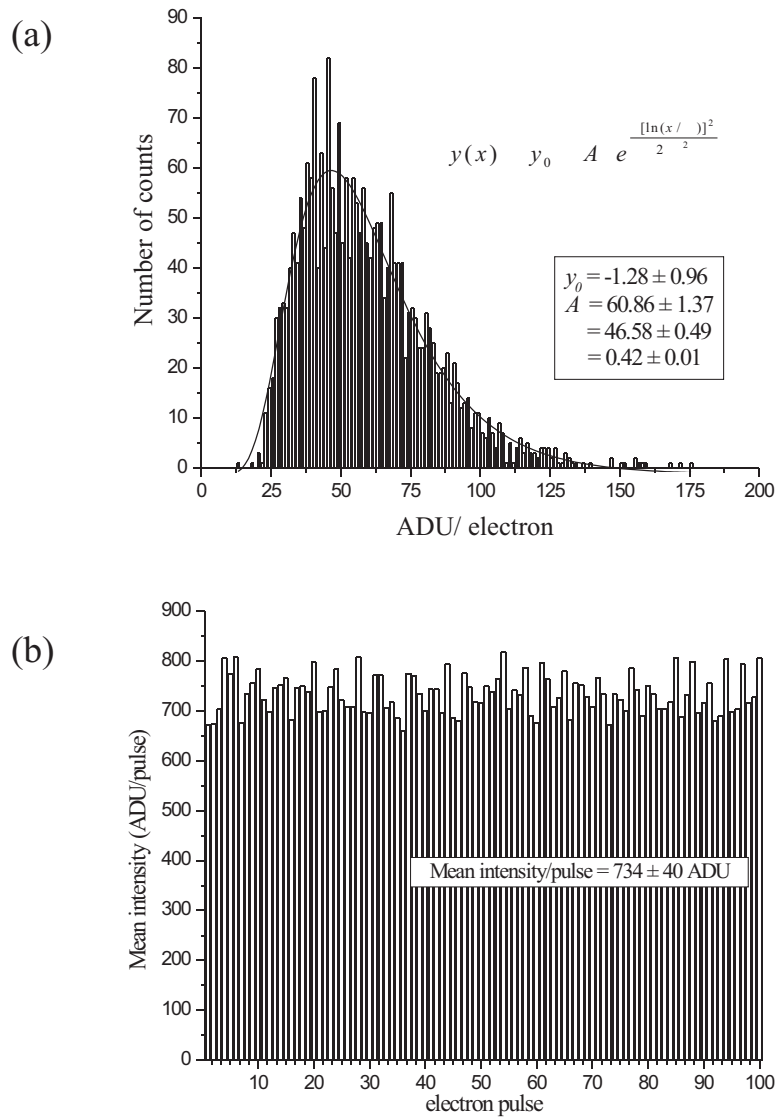


Fig. 3-10. (a) The intensities of single electrons on the detector fit with a log-normal distribution. The mean value provides the response of the detector to a single electron and is needed in the calibration of the experiment. (b) Intensities of pulses of electrons showing the shot-to-shot stability in the number of electrons over 100 pulses.

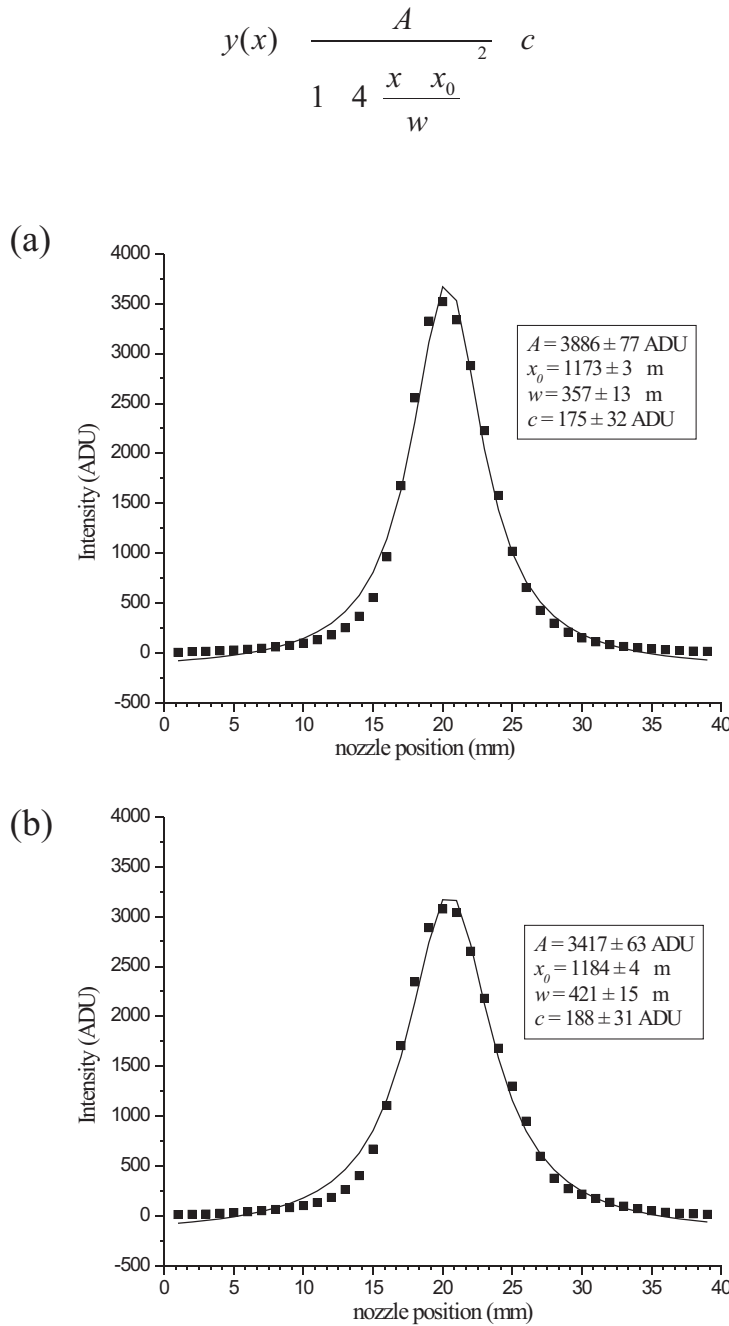


Fig. 3-11. (a) Vertical and (b) horizontal intensity profiles of an electron pulse. The data shown is the average of 100 pulses and each profile is fit with the Lorentzian distribution shown at the top.

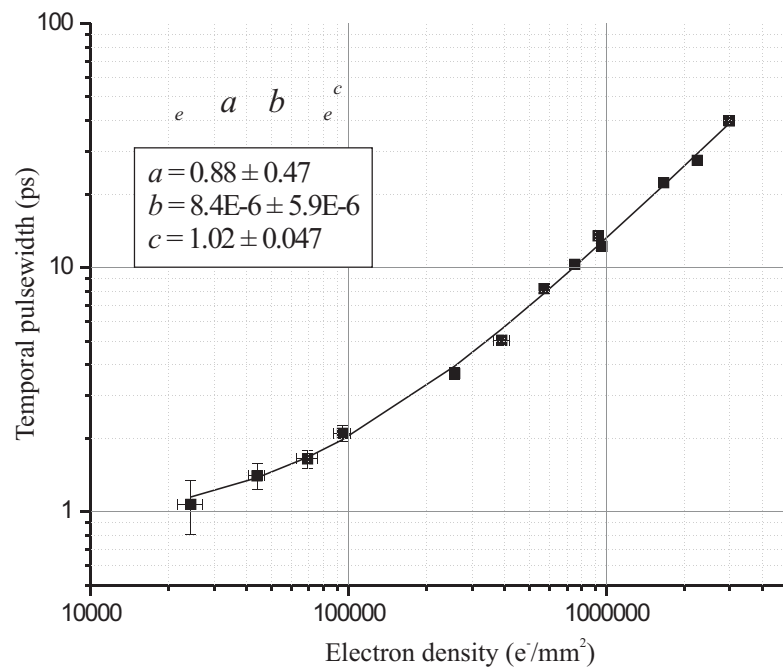


Fig. 3-12. The correlation between the electron density of UED electron pulses and those pulses' temporal widths. Electron density is calculated by dividing the number of electrons per pulse by the FWHM area on the detector.

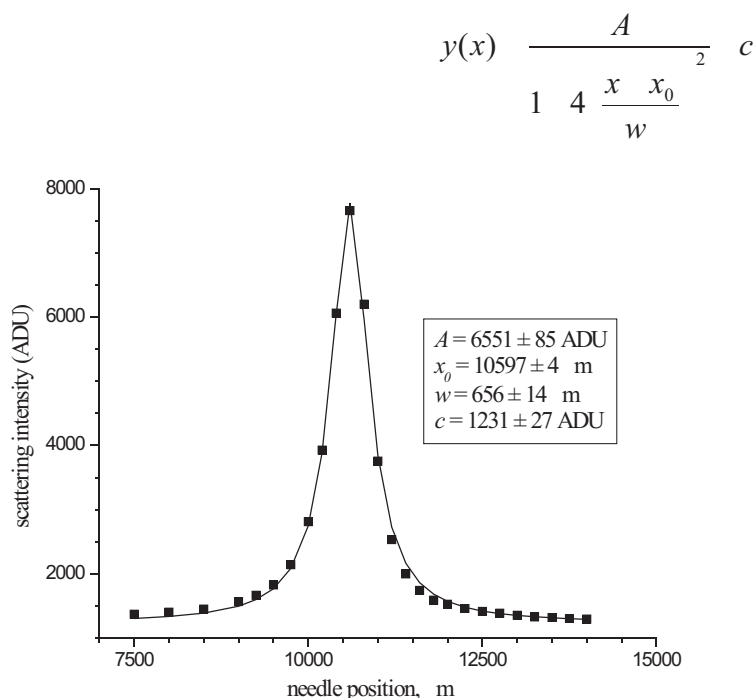


Fig. 3-13. Molecular beam size measurement. Scattering intensity as a function of molecular beam position along the axis perpendicular to the electron beam (parallel with the excitation laser). The data is fit with a Lorentzian distribution from which the width of the molecular beam may be deconvoluted. The distribution also supplies the position of maximum overlap between electron and molecular beams.

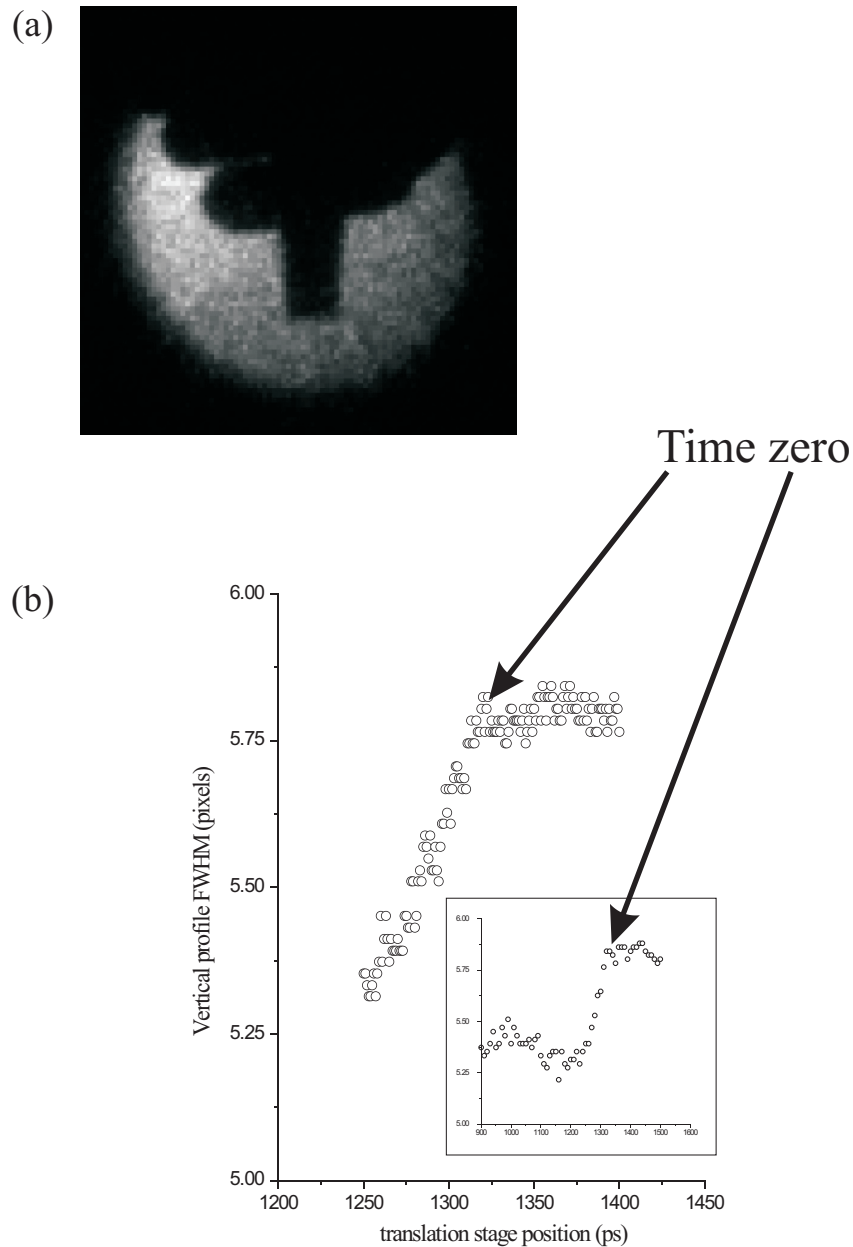


Fig. 3-14. Beam alignment and zero-of-time determination. (a) The shadow of the needle as seen on the detector with the defocused electron beam. Rough alignment of the laser beam to the needle is done in a similar way by viewing the needle shadow after the Brewster outlet window. (b) Lensing measurements showing the change in vertical profile of the electron beam as a function of the excitation laser delay time. Time zero is marked as the point at which the electron beam vertically contracts. The inset is a coarser scan showing the vertical profile change over a wider range of time points.

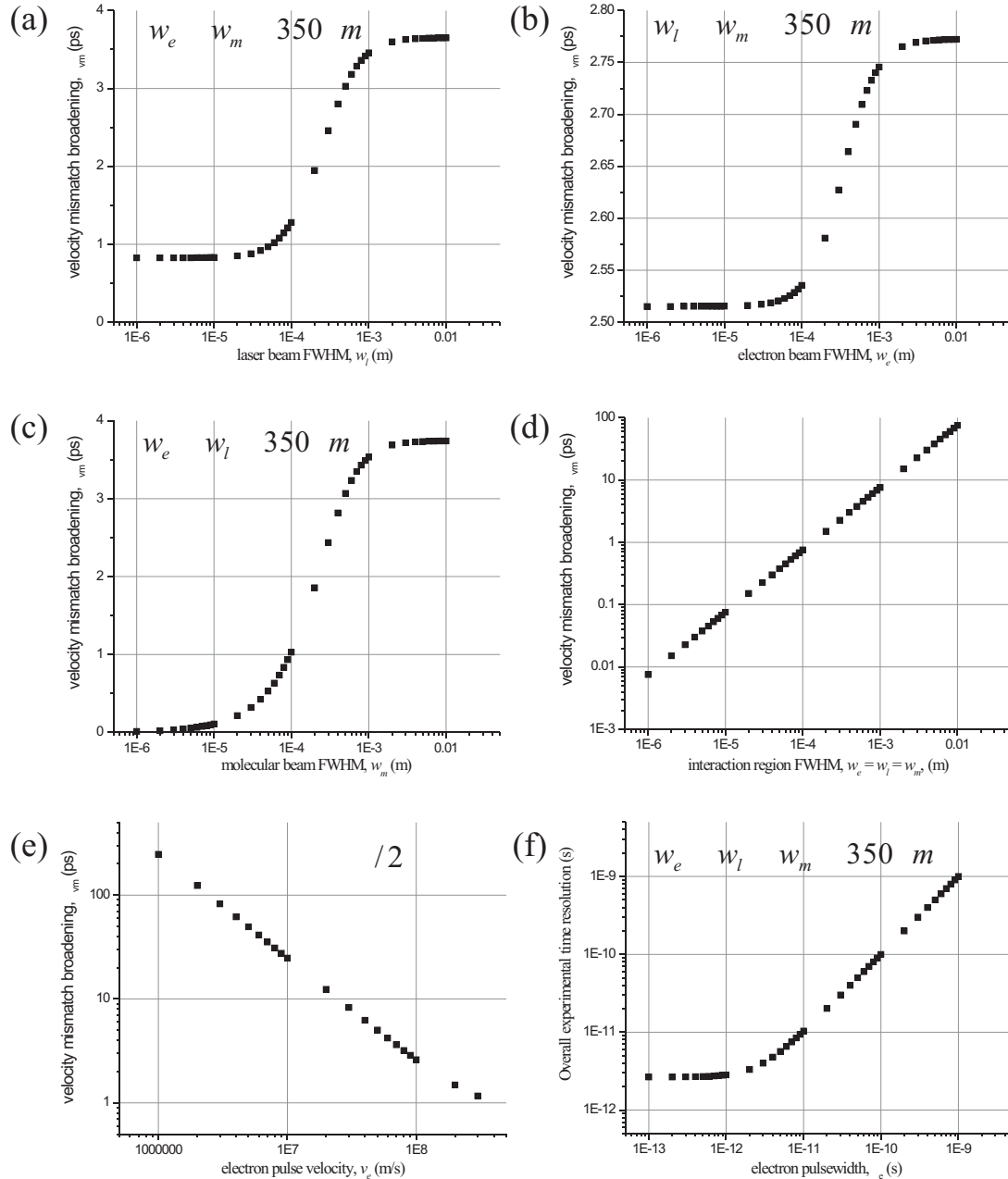


Fig. 3-15. The dependency of the temporal broadening due to velocity mismatch when (a) the spatial width of the laser is varied, (b) the spatial width of the electron beam is varied, (c) the spatial width of the molecular beam is varied, (d) the spatial widths of all three beams are varied while remaining equal to one another, (e) the velocity of the electron pulses are varied while the laser beam and electron beam intersect the molecular beam (all $w = 350$ mm) in a mutually perpendicular arrangement. (f) The overall experimental time resolution as a function of the electron pulselength.